Semianalytical Characterization of Turbulence from Radial Impellers, with Experimental and Numerical Validation

Ronen Ben-Nun and Moshe Sheintuch
Dept. of Chemical Engineering, Technion – Israel Institute of Technology, Haifa, Israel 3200003

Bohuš Kysela and Jiří Konfršt
Institute of Hydrodynamics AS CR, v. v. i., Prague, Czech Republic

Ivan Fořt
Dept. of Process Engineering, Faculty of Mechanical Engineering, Czech Technical University in Prague, Prague, Czech Republic

DOI 10.1002/aic.14723

Based on conventional turbulent jet theory and the general theoretical framework of scalar dispersion in turbulent shear flows, a novel formulation of the radial impeller's jet in stirred tanks is introduced. Whereas previous studies considered the impeller's jet as developed, it is now comprised of two separate spatial regions along the radial axis: the zone of flow establishment (ZFE) and the zone of established flow (ZEF). This formulation is accompanied with semi-analytical expressions for the prediction of turbulent key parameters including the random part of k and ε in the ZFE. The new theoretical framework is validated both with laser Doppler anemometry measurements and with 3-D numerical simulations using the standard $k-\varepsilon$ turbulent model. © 2015 American Institute of Chemical Engineers *AIChE J*, 61: 1413–1426, 2015
Keywords: turbulent jet, mixing, radial impeller, stirred tank, Rushton turbine

Introduction

Stirred tanks serve a wide range of industrial applications, ranging from basic tasks such as homogenization[1–3] to more complex scenarios involving solid suspensions,[4–6] crystallizations,[7,8] bioreactions,[9,10] and so forth. In most of the cases, the ability to understand, predict, and even control the flowfields of such systems impacts and improves the performance and profitability of a given process.[11]

Among the efforts in this field, the Rushton turbine used in the standard stirred tank configuration has received great attention.[12–14] This is due to the relatively simple geometry of the system and the expectation that it may lead to general understandings of the entire class of radial impellers. Radial impellers pump fluid along the axial direction and discharge that fluid in the radial direction. The discharge zone has relatively high mixing rates, and, as such, is of great industrial importance. As a consequence, this zone has been the focus of many studies which characterized it, both experimentally and numerically.[15–17] However, given the long timeframe of existing numerical and experimental studies on one hand and the industrial requirement for quick and accurate predictions on the other hand, we advocate that there is real value in approximate solutions, such as those introduced in this article.

The connection between swirling-radial-jets and radial impellers was pointed out long ago.[18,19] This concept was further developed with time and has been applied for complex geometries such as stirred tanks.[20–22] However, most of the models predict only the velocity field (e.g., the swirling-radial-jet model[23,24]). In 1991, the swirling-radial-jet model was extended numerically to provide the k and ε turbulent parameters as well.[25] This was done by including the standard $k-\varepsilon$ turbulent model under the radial-jet approximations. Although such a model seemed to demonstrate good agreement with experimental results,[25] the experimental data chosen for comparison actually included the pseudoturbulence[26]—periodic velocity fluctuations which are created by the periodic motion of the impeller. As turbulence theory is mainly based on random fluctuations, the periodic fluctuations should have been decomposed from the total fluctuations before comparison with the model prediction (for review on decomposition techniques the reader is referred to Escudie and Line[27]). As a consequence, the underline physical phenomenon, the existence of the initial evolvement region of the jet, was unnoticed and the impeller's jet was addressed as developed. The evolvement region is of high significance as it creates a coordinate shift in the location from which the turbulent parameters can be predicted by these models. Disregarding its existence by extrapolating from the impeller's tip, as has been done thus far, results in an inherent physical error which can be avoided. Moreover, as will be shown in this work, this correction enabled us to develop semianalytical expressions for the prediction of the random turbulence in this region.

The main aim of the present work is to present a new view of the radial impeller's jet, by introducing the initial

---

Correspondence concerning this article should be addressed to R. Ben-Nun at rbn@tx.technion.ac.il.

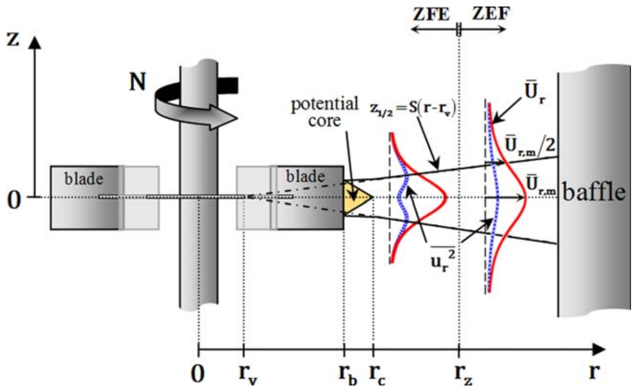

Figure 1. Schematic presentation of the jet formed by the impeller illustrating the axial-distribution profiles of $\bar{U}_r$ and $\overline{u_r^2}$ at the evolving and evolved regions along with the coordinate system and notation used in this work.

[Color figure can be viewed in the online issue, which is available at wileyonlinelibrary.com.]

evolvement region and thus providing physical correction to existing models. As we show here, the random turbulence characteristics in the evolvement region (k and ε) can be predicted in a semianalytical form. Such information can be used for industrial design purposes, compared with experimental results, and implemented in models of local mixing rates (e.g., predicting the reaction rate in a reactive flow with reactants fed in the vicinity of the discharge jet).

The outline of this work is as follows: in the "Theoretical Approach" section, we introduce a novel view of the radial impeller's jet as composed of two separate spatial regions, each with different turbulent characteristics: the zone of flow establishment (ZFE) and the zone of established flow (ZEF).[28] The former region has been ignored in previous studies. Based on this formulation and the general theoretical framework of scalar dispersion in turbulent shear flows, we develop semianalytical expressions for the prediction of the random turbulent parameters k and ε in the ZFE. In the "Methodology" section, we describe our process for validating our theoretical work, both with experimental laser Doppler anemometry (LDA) measurements, and with three-dimentional (3-D) numerical simulations using the standard $k-\varepsilon$ turbulent model. In the "Results and Discussion" section, we successfully identify the experimental existence of the ZFE and ZEF regions, and further demonstrate our ability to predict the random turbulence within the ZFE region. Finally, in our "Summary" section, we conclude with a rejoinder emphasizing the industrial applications and pertinence of our approach.

Theoretical Approach

In Figure 1, we portray the system structure including the potential core (see definition below), the ZFE and the ZEF, as well as the impeller and baffles; the spreading rate, the axial-distribution profiles of the averaged radial velocity ($\bar{U}_r(z)$) and of the normal Reynolds-stress in the radial direction ($\overline{u_r^2}$) are also denoted.[28] In the following sections we elaborate on this view.

The discharge flow, a wake or a jet?

The flow created by radial impellers can be visualized as a combination of two basic types of flow: wake and jet. The wake is the downstream flow region created by fluid motion over an obstacle or body motion in a fluid surrounding, in our case the motion of the blades. The wake type of flow is characterized by velocity/momentum defect profile. The jet is the flow region created by fluid injection into a surrounding fluid, in our case the injection of fluid in the radial direction. The jet type of flow is characterized by velocity/momentum excess profile. In general, as the number of blades installed on the impeller increases, the wake type of flow weakens whereas the jet type of flow strengthens, and vice versa. We restrict our discussion to cases where the flow characteristics are dominated by the jet type of flow, as in the case of the six-blade Rushton impeller (see Figure 2).

Characterizing the impeller's jet as a simple radial-jet with no swirl

We adopt the common simplifying assumptions for the impeller's jet: (1) incompressible fluid, (2) high Reynolds numbers, implying that the flow regime is fully turbulent, a reasonable assumption for practical situations. (3) Statistically steady flow. (4) Statistically axisymmetric flow; as will be shown later on, the relative error introduced by this assumption is relatively modest for the majority of the jet domain (see section "Numerical examination of the axisymmetric assumption"). (5) Boundary layer approximation, implying that the dominant physical mechanism is convection in the radial direction whereas turbulent diffusion is the dominant physical mechanism in the axial direction. (6) Constant turbulent viscosity (7) free turbulent jet, implying that

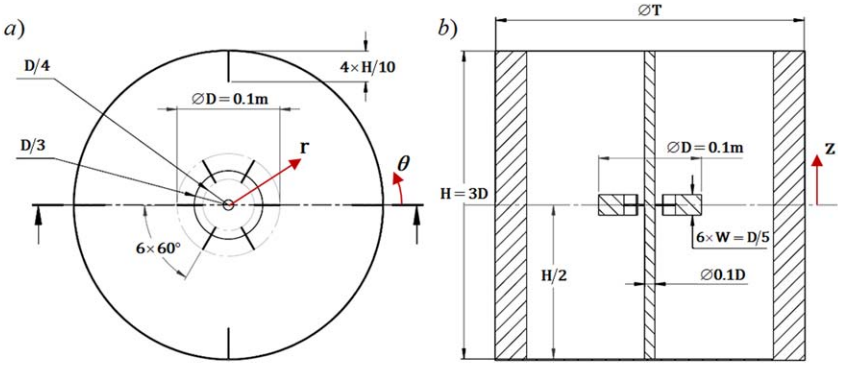

Figure 2. Geometry and dimensions of the virtual stirred tank system (a) top view and (b) side view.

[Color figure can be viewed in the online issue, which is available at wileyonlinelibrary.com.]

the flow is remote from walls hence, the flow evolvement is not affected by them. (8) Quiescent ambient fluid.

Following these assumptions, the governing equations are reduced to the basic swirling-radial-jet equations.[25] Based on a unique coordinate transformation which was basically developed for the laminar case,[18] these equations can be further reduced to the basic turbulent radial-jet equations with no swirl in a direction tangent to a cylinder of radius "e", $(r,\theta,z) \rightarrow \left(\sqrt{r^2-e^2}, z\right)$. The cylinder radius is determined by the asymptotic ratio of the radial to angular momentum flux in the radial direction.[23,25]

After solving the transformed equations and retransforming the solution to the regular cylindrical coordinate system, it can be seen that the description of the jet properties relative to the radial direction remains the same as in the simple radial-jet case (see "Appendix"). This insight is of importance as it enables us to obtain the evolvement of the jet properties in the radial direction by characterizing the impeller's jet as a simple radial-jet with no swirl (in the radial direction) thus avoiding using the unknown parameter e, as portrayed in Figure 1. It should be stressed that by applying this approach, we do not mean that the flow does not have a swirl component. Furthermore, our numerical results indicated that for large tank to impeller diameter ratios where the effect of the baffles is reduced and the fluid starts to swirl along with the impeller, the parameter e varied significantly along the radial position and thus cannot be considered as constant as was so far done. Therefore, our prediction should be also applicable to baffles-free stirred tanks which in certain industrial applications are more common than the baffled ones.[29] Moreover, the statistical axisymmetric description of the flow implies that convection along the angular coordinate is of minor importance, whereas the convection along the radial coordinate is of prime importance. Note that the latter also determines the residence time in this region.

Distinction between the ZFE and ZEF regions

The concept of ZEF and ZFE regions originated in the jet-theory literature.[30–32] In this theory, it is generally known that as the considered statistical flow-field variable is a moment of higher order (e.g., $\bar{U}_r$ and $\overline{u_r{}^2}$ are moments of first and second order, respectively), it becomes self-similar at higher distances from the nozzle exit.[33] For clarity, the term "self-similar" relates to the case where the mean axial-distribution profiles of the flow-field parameters at different longitudinal positions (radial position in our case) can collapse into a single profile, after normalization with the local characteristic velocity and length scales. Hence, we divide the impeller's jet by two characteristic points: the boundary of the potential core (r_c) and the boundary of the ZEF (r_z). These boundaries indicate the radial location beyond which $\bar{U}_r$ and $\overline{u_r{}^2}$ can be regarded as self-similar, respectively. In other words, the impeller's jet is divided into two zones: (1) in the first, at least one of the jet's axial-distribution profiles of $\bar{U}_r$ and $\overline{u_r{}^2}$ is not evolved (ZFE, $r_b < r < r_z$); (2) in the second, both $\bar{U}_r$ and $\overline{u_r{}^2}$ are in their final self-similar axial-distribution profiles (ZEF, $r_z < r$). The first (ZFE) is further divided into two regions: in the first, the axial-distribution profile of $\bar{U}_r$ still evolves ($r_b < r < r_c$) whereas in the second, $\bar{U}_r$ is fully developed and $\overline{u_r{}^2}$ still evolves to its final self-similar axial-distribution profile ($r_c < r < r_z$).

Review of definitions and main relevant results in the ZEF (r_z<r)

The jet's half-width is defined as the axial position $z{=}z_{1/2}$ where

$$\bar{U}_r\big|_{\left(r,z_{1/2}\right)}=0.5\bar{U}_r\big|_{(r,0)}=0.5\bar{U}_{r,m} \tag{1}$$

The spreading rate of the radial-jets (S) is usually defined as the slope of change of half-width[34]

$$S=\frac{d\left(z_{1/2}\right)}{dr} \tag{2}$$

The spreading rate is usually regarded as constant for specific geometry, independent of Reynolds number. In other words, the jet's half-width grows linearly with the radial position as can be obtained by integrating Eq. 2

$$z_{1/2}=S(r-r_v) \tag{3}$$

Here, r_v represents the virtual origin which defines the radial location where the interpolated jet's half-width is zero (see Figure 1).

In order for the free radial turbulent jet equations to become self-similar the following terms should be sustained[35]

$$\bar{U}_{r,m} \propto r^{-1}\ ;\quad z_{1/2}=S(r-r_v)\ ;\quad r_v \ll r \tag{4}$$

The condition $r_v \ll r$ is unique to the radial-jet configuration. In similarity to previous work in which the $k-\varepsilon$ turbulence model was used to expand the swirling-radial-jet model,[25] the evolution of k and ε at the centerline of the jet (k_m and ε_m) can be deduced as well. Hence, based on the self-similar assumption along with Eq. 4 one obtains

$$\bar{U}_{r,m}=\bar{U}_{r,m,0}\left(\frac{r_0}{r}\right)\ ;\quad k_m=k_{m,0}\left(\frac{r_0}{r}\right)^2;\ \varepsilon_m=\varepsilon_{m,0}\left(\frac{r_0}{r}\right)^4 \tag{5}$$

where the sub index "0" refers to a radial location r_0 which is depicted inside the ZEF ($r_0 > r_z$). Solving the radial-jet's equations based on assumptions (1)–(8) along with the self-similarity assumption results with the common self-similar profile[34]

$$\frac{\bar{U}_r}{\bar{U}_{r,m}}=\operatorname{sech}^2\left(0.881\frac{z}{z_{1/2}}\right) \tag{6}$$

In addition, it can be shown that the turbulent viscosity can be represented by (see "Appendix")

$$\nu_T=\frac{S\cdot\bar{U}_{r,m}\cdot z_{1/2}}{2(0.881)^2} \tag{7}$$

Prediction of the turbulent parameters in the ZFE (r_b<r<r_z)

Prediction of $\bar{U}_r$. The evolvement of $\bar{U}_r$ is divided by the potential core boundary (r_c). The potential core is a region, close to the nozzle (impeller blades in our case), where the averaged exit velocity of the jet remains constant. The lateral width of the potential core reduces with the longitudinal coordinate as the boundary layers penetrate inward toward the centerline of the jet. The point where the boundary layers merge and the averaged lateral velocity at the centerline of the jet starts to decline and the jet's half-width grows linearly with the radial position is identified as the boundary of the potential core (denoted by r_c). This can be expressed mathematically by

$$\bar{U}_{r,m}=\begin{cases}\bar{U}_{r,m,b} & \text{for} \quad r_b \le r \le r_c \\ \bar{U}_{r,m,b}\left(\dfrac{r_c}{r}\right) & \text{for} \quad r_c \le r\end{cases} \tag{8}$$

$$z_{1/2}=\begin{cases}S(r_c-r_v) & \text{for} \quad r_b \le r \le r_c \\ S(r-r_v) & \text{for} \quad r_c \le r\end{cases} \tag{9}$$

Experimental observations indicate that r_c is approximately five to six times the nozzle width, from which the jet emerge, usually measured starting from the virtual origin.[36] However, there is an essential geometrical difference between common radial-jet configurations and the radial impeller. Whereas, the former is usually created by two closely spaced parallel circular disks which are impermeable to fluid from the axial direction, the radial impeller configuration is axially open. This implies that the averaged exit axial-distribution profile of the radial velocity should be relatively developed at the impeller tip and thus, $\bar{U}_r$ can be evaluated according to Eq. 6. Moreover, r_c is expected to be very close to the impeller tip (r_b) independent of impeller's blade width and rotational speed. Hence, for practical cases where r_c is unknown, a first good evaluation of $\bar{U}_r$ would be to assume a negligible potential core so that the mean radial velocity can be described by Eqs. 4–6 starting from the impeller tip

$$\bar{U}_{r,m}=\bar{U}_{r,m,b}\left(\frac{r_b}{r}\right); \qquad \frac{\bar{U}_r}{\bar{U}_{r,m}}=\operatorname{sech}^2\left(0.881\frac{z}{z_{1/2}}\right) \tag{10}$$

where $\bar{U}_{r,m,b}$ is the maximal radial velocity at the impeller tip which can be related to the impeller's pumping number ($N_q=Q_p/ND^3$) by integrating the radial velocity profile according to

$$Q_p=\int_{-W/2}^{W/2}\bar{U}_{r,m,b}\operatorname{sech}^2\left(0.881\frac{z}{z_{1/2}}\right)dz \tag{11}$$

Whereas, for this purpose, it is reasonable to take $z_{1/2}$ to be equal to $W/4$. Substituting into Eq. 11 and rearranging yields

$$\bar{U}_{r,m,b}=0.2V_{\text{tip}}N_q\left(\frac{D}{W}\right) \tag{12}$$

Considering the Rushton six-blade standard turbine ($D/W=5$) with $N_q=0.75$ one obtains $\bar{U}_{r,m,b}=0.75V_{\text{tip}}$ which agrees well with experimental results.[37]

Prediction of k and ε. In this section, we develop semi-analytical expressions for k and ε based on the shape variation of the axial-distribution profiles of $\overline{u_r^2}$ (see Figure 1). We start with the general theoretical framework of scalar dispersion in turbulent shear flows to derive the axial-distribution profiles of $\overline{u_r^2}$.

Consider the case of scalar dispersion in free shear turbulent flow where the scalar is emanating from a uniform scalar source of value θ_1. Then, under the assumption of negligible molecular diffusion, the probability density function (p.d.f) of the scalar should have the following familiar form[38]

$$p(\theta;x,t)=\pi(x,t)\delta(\theta-\theta_1)+\{1-\pi(x,t)\}\delta(\theta) \tag{13}$$

where $\pi(x,t)$ is the intermittency factor, that is, the probability that the flow at a specific location and time is turbulent. Note that turbulent free shear flows are known to be intermittent toward the edge, that is, the flow is turbulent and nonturbulent, intermittently. Using basic definitions of statistical analysis, the mean value of the scalar (C) and its mean square fluctuation (c^2) can be easily derived to provide[38]

$$C=\theta_1\pi \qquad ; \qquad c^2=\theta_1^2\pi(1-\pi) \tag{14}$$

Then, by eliminating π, one obtains[38]

$$c^2=\left(\frac{1}{2}\theta_1\right)^2-\left(C-\frac{1}{2}\theta_1\right)^2 \tag{15}$$

The same procedure can be applied to the radial velocity. Therefore, by replacing the molecular diffusion, C and c^2 with the molecular viscosity (ν), $\bar{U}_r$ and $\overline{u_r^2}$, respectively, and θ_1 with the maximal radial velocity at the impeller tip ($\bar{U}_{r,m,b}$) one finds

$$\overline{u_r^2}=A_u\left[\left(\frac{1}{2}\bar{U}_{r,m,b}\right)^2-\left(\bar{U}_r-\frac{1}{2}\bar{U}_{r,m,b}\right)^2\right]=A_u f(\bar{U}_r) \tag{16}$$

where here, we introduced coefficient of proportionality for $\overline{u_r^2}$, A_u. From Eqs. 10 and 16, it follows that $\overline{u_r^2}$ has a maximum value of $\frac{1}{4}A_u\bar{U}_{r,m,b}$ at $\bar{U}_r(r,z)=\frac{1}{2}\bar{U}_{r,m,b}$. Thus, $\overline{u_r^2}$ exhibits two different axial-distribution profiles with three or one extrema points before and after $r=2r_b$ as presented schematically in Figure 1. As the ZFE is the region where the exit axial-distribution profiles develop to the final similarity profiles of the ZEF, it is expected that $r=2r_b$ can serve as a coarse estimation for r_z. This implies that for practical stirred tank geometry (e.g., $T/D=3$, $r/r_b \le 3$), the evolvement region spans over a significant portion of the impellers jet, and thus should not be neglected.

Assuming that the turbulent kinetic energy (k) is proportional to $\overline{u_r^2}$ one obtains

$$k=A_k f(\bar{U}_r) \tag{17}$$

where A_k is the coefficient of proportionality for k which can be assessed and bounded by simple assumptions. Considering that the largest contribution to k comes from $\overline{u_r^2}$ then by assuming a 3-D isotropic turbulence, that is, $\overline{u_r^2}=\overline{u_\theta^2}=\overline{u_z^2}$ and on the other hand by neglecting the two other components, that is, $\overline{u_r^2} \gg \overline{u_\theta^2}, \overline{u_z^2}$ one obtains the upper and lower bounds for A_k, respectively. It follows that $0.5A_u < A_k < 1.5A_u$. Based on dimensional analysis and Eq. 17 ($\varepsilon \propto k^{3/2}/z_{1/2}$) the expression for ε takes the following form

$$\varepsilon=A_\varepsilon f(\bar{U}_r)^{3/2}/z_{1/2} \tag{18}$$

where A_ε is the coefficient of proportionality for ε which is assessed by $A_\varepsilon \approx (A_k)^{3/2}$ as the proportionality coefficient for the dimensional analysis is known to be of order unity.[39]

Concluding this section, we portray the impeller's jet as composed of two main regions: the ZFE and the ZEF. The ZFE is the region where the axial-distribution profiles of the turbulent statistical-moments of first and second order, evolve to their self-similar shape. The ZEF is the region where both the first and second statistical-moments can be considered as self-similar. In Tables 1 and 2, we summarized the model prediction of the turbulent flow-field properties in these regions: few measurements in the impellers discharge zone are sufficient to write an analytical prediction to the turbulent flow-field both in the ZFE and the ZEF.

Table 1. Summary of Model Prediction in the ZFE $(r_b \leq r \leq r_z)$

Turbulent Parameter	Model Prediction	Empirical Parameter Required	Comments	Comparison To Experimental Data
$\bar{U}_r$	$\frac{\bar{U}_r}{\bar{U}_{r,m}}=sech^2\left(0.881\frac{z}{z_{1/2}}\right)$ where $\bar{U}_{r,m}=\begin{cases}\bar{U}_{r,m,b} & \text{for} \quad r_b \leq r \leq r_c \\ \bar{U}_{r,m,b}\left(\frac{r_c}{r}\right) & \text{for} \quad r_c \leq r\end{cases}$ and $z_{1/2}=\begin{cases}S(r_c-r_v) & \text{for} \quad r_b \leq r \leq r_c \\ S(r-r_v) & \text{for} \quad r_c \leq r\end{cases}$	$\bar{U}_{r,m,b}$ and $z_{1/2}$ which depends on: $S, \quad r_c, \quad r_v$	For coarse evaluation and in cases where experimental data are lacking neglect r_v and r_c, that is, $\frac{\bar{U}_r}{\bar{U}_{r,m}}=sech^2\left(0.881\frac{z}{z_{1/2}}\right)$ where $\bar{U}_{r,m}=\bar{U}_{r,m,b}\left(\frac{r_b}{r}\right)$ $z_{1/2}=0.12 \cdot r$ and $\bar{U}_{r,m,b}=0.2V_{\text{tip}}N_{\text{q}}\left(\frac{D}{W}\right)$	Figures 8–10
$\bar{u}_r^2$	$\bar{u}_r^2=A_u\left[\left(\frac{1}{2}\bar{U}_{r,m,b}\right)^2-\left(\bar{U}_r-\frac{1}{2}\bar{U}_{r,m,b}\right)^2\right]=A_uf(\bar{U}_r)$	A_u		Figure 11
k	$k=A_kf(\bar{U}_r)$	A_k	$0.5A_u < A_k < 1.5A_u$	Figure 12
ε	$\varepsilon=A_\varepsilon f(\bar{U}_r)^{3/2}/z_{1/2}$	A_ε	$A_\varepsilon \approx (A_k)^{3/2}$	Figure 12

Methodology

The model prediction was validated against experimental and numerical results. In the following, we elaborate on each of the methods used.

Simulation details

The model prediction was validated over a wide range of 3-D numerical simulations of stirred tank. To reduce computational requirements, we run steady-state calculations, refined the mesh locally based on the results, and averaged the final results over the angular coordinate. Then, the averaged results were analyzed to characterize the impeller's jet, as illustrated in Figure 1. In the following, we elaborate on the methodology used.

The tank simulated was a flat-bottom cylindrical vessel equipped with four equally spaced baffles. The standard six-blade Rushton turbine ($D/W=5$) was placed at the middle of the tank ($C=H/2$) parallel to the tank bottom as presented in Figure 2. The thickness of the baffles, blades, and the impeller's disk were all set to be $0.01D$ whereas $D=0.1$m. With this configuration, the rotational speed was varied from 100 to 1600 rpm at $T/D=3$. The free jet assumption was also examined by additional numerical case in which the tank to impeller diameter ratio was varied from three to nine ($D=0.1$m) while all the other geometrical ratios where kept the same and the rotational speed was set to 1600 rpm (see Figure 3). The impeller's Reynolds number ($Re=ND^2/\nu$) varied from 1.67×10^4 to 2.67×10^5, corresponding to rotational speeds of 100 and 1600 rpm, respectively ($\nu=10^{-6}$ m^2 s^{-1}). Therefore, all simulations were considered to be in the turbulent region ($Re > 10^4$ for water at room temperature[40,41]).

The simulations were performed using the commercial software Fluent V.14. To avoid time consuming transient calculations, we conducted steady-state calculations where the averaged flow-field is calculated for a specific orientation of the impeller blades relative to the baffles (one of the blades was set to be parallel to one of the baffles). The models used were the multiple reference frame model[42] along with the standard $k-\varepsilon$ turbulence model[43] (with the standard values of the model constants) and the standard wall functions,[44] models which were previously examined to provide accurate results for this system.[25] To improve the accuracy of the results and to reduce computational requirements, the numerical grid was refined locally several times based on the results. The final grid ranged from six to nine million cells and was significantly higher than the recommended value for mesh independent solution for the averaged velocity field while using the above models.[45,46] For example, the final grid used at the impeller horizontal midplane of the $T/D=3$

Table 2. Summary of Model Prediction in the ZEF $(r_z \leq r)$

Turbulent Parameter	Model Prediction	Empirical Parameter Required	Comments	Comparison to Simulation Data
$\bar{U}_r$	Same prediction as in the ZFE			Figures 8–10
ν_T	$\nu_T=\frac{S \cdot \bar{U}_{r,m} \cdot z_{1/2}}{2(0.881)^2}$	$\bar{U}_{r,m,b}$ and $z_{1/2}$ which depends on: $S, \quad r_c, \quad r_v$	Sensitive to the spreading rate (S)	
k	$k_m=k_{m,0}\left(\frac{r_0}{r}\right)^2$	$k_{m,0}$	The self similar axial distribution profile should fit the suggested numerical solution given by Kresta and Wood[25] whereas $k_{m,0}$ should be determined experimentally	Figure 13
ε	$\varepsilon_m=\varepsilon_{m,0}\left(\frac{r_0}{r}\right)^4$	$\varepsilon_{m,0}$	Same comment as for k. Note that $\varepsilon_{m,0}$ can be evaluated from ν_T and k_m while assuming that $\nu_T=C_\mu k^2/\varepsilon$ whereas C_μ should be equal to the common value (0.09)	Figure 14

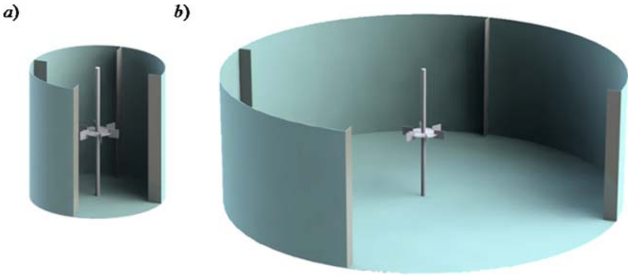

Figure 3. Schematic presentation of the virtual stirred tank system (a) T/D=3 and (b) T/D=9.

[Color figure can be viewed in the online issue, which is available at wileyonlinelibrary.com.]

case is given in Figure 4 showing denser grid near the tank walls, baffles, impeller blades, and their trails, as expected. Then, the results were averaged over the angular coordinate and analyzed to characterize the impeller's discharge zone using common definitions of turbulent jets (e.g., jet's half-width, spreading rate, velocity decay rate, etc.) as illustrated in Figure 1.

Important remarks:

1. To verify that the results dependency on the relative orientation of the impeller is negligible, we ran and compared two steady-state simulations differing only in the impeller-baffles relative orientation. To account for the maximal impeller-baffles relative orientation effect, we set the two cases to have the maximal geometrical difference, which is 15° in the impeller orientation, and choose the $T/D=3$ geometry with rotational speed of 1600 rpm. In one of the cases, one of the impeller blades was set to be parallel to one of the baffles as stated above. The results averaged over the angular coordinate showed small difference: up to 0.25% for the velocity field and up to 2% for both k and ε fields thus indicating that the results dependency on the impeller orientation is negligible.
2. The procedure above is applicable for obtaining the averaged radial velocity in the axisymmetric region thanks to the statistical axisymmetry of the flow and the fact that the periodic velocity fluctuations do not change the averaged velocity flow-field (under definition).
3. The procedure above is applicable for obtaining the k and ε parameteres in the region beyond $r/r_b=1.6$ where the pseudoturbulence is known to be negligible.[39] Note that in the region up to $r/r_b=1.6$, the k and ε numerical results include the pseudoturbulence and thus under this procedure the validity of Eqs. 16–18 is not traceable. Nevertheless, this will be done using experimental data.

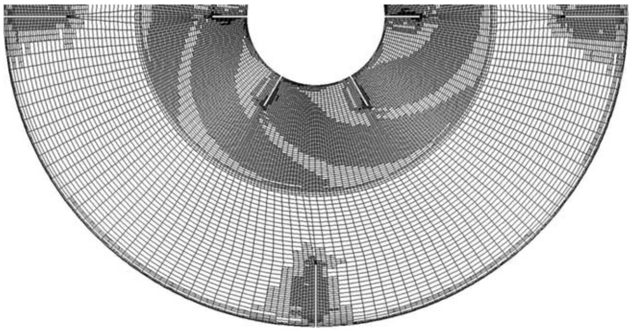

Figure 4. Presentation of the final numerical grid used for the T/D=3 case at the impeller horizontal midplane (z=0) after local grid refinement on results basis.

Experimental details

The geometry of the experimental system used in this work was based on the $T/D=3$ numerical configuration ($T=0.3$m). The baffles and impeller thickness of the experimental system were $0.02D$ and $0.015D$, respectively. To prevent vortex effects, the tank was closed at the top using a lid. To reduce temperature change of the working fluid (distilled water at 19°C), the tank was placed inside a cubical vessel filled with water. The rotational speeds used were of 200 and 400 rpm corresponding to $Re=3.33\times10^4$ and 6.66×10^4, respectively.

Continuous time LDA measurements of the radial velocity were taken at the vertical plane between two baffles $\left(r, 45^0, z\right)$ thus providing eight axial-distribution profiles, located at different radial positions, each composed of 21 measurements points. The LDA system setup consisted of Coherent INNOVA 305Ion-Argon laser beam with wavelength of 514 nm and power supply of 5 W. The measured volume was an ellipsoid with diameter and length of 8.6×10^{-5} and 7.1×10^{-4}m, respectively—small enough to capture the energy-containing range and inertial subrange of turbulence ($>60l_k$ where l_k is the Kolmogorove length scale[47]; in our case, l_k is on the order of 10^{-5}m for both of the rotational speeds based on $l_k \sim D \cdot Re^{-3/4}$).

To reduce optical distortion, the laser beams went through the flat bottom of the vessel. The trace particles were Silver coated—Hollow Glass Spheres (S-HGS) with mean diameter of 10 µm and density of 1100 kg m^{-3} which is close to the density of the working fluid. In each measurement, about 25 K instantaneous velocity values were acquired in the single measurement burst mode.

To account for the pseudoturbulence, the velocity signal was triple-decomposed into time-mean, periodic part, and random part[48] using Wu and Patterson[39] autocorrelation decomposition technique. In the following, only the time-mean and random parts are analyzed and presented.

Results and Discussion

In this section, we examine and validate our novel view using experimental and numerical results as illustrated in Figure 1. The comparison is divided into three sections: prediction of the averaged radial velocity, prediction of $\overline{u_r^2}$, k,and ε in the ZFE, and prediction of v_T, k,and ε in the ZEF.

It should be noted that we recently found (numerically) that multiple solutions may exist for a sufficiently large T/D ratio (e.g., $4 \le T/D$ for the investigated system) with a symmetric solution (relative to the impeller horizontal midplane, $z=0$) that may become unstable and two stable asymmetrical mirror-image solutions where the impeller's jet is significantly inclined upward or downward ($\pm z$), as in the case where the impeller is installed close to the tank bottom[49,50] or the liquid level[51] (as we showed elsewhere[52]). Here, we consider only the symmetric solution.

Numerical examination of the axisymmetric assumption

The axisymmetry of system domain is broken by the blades and baffles and those constitute a source for flow deviations along the angular coordinate. To illustrate this point, we present in Figure 5 the contours of the ensemble-

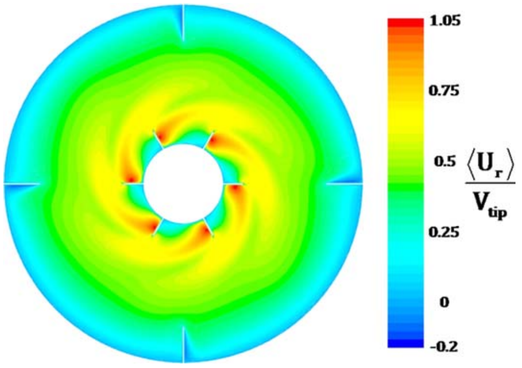

Figure 5. Contours of the ensemble-averaged radial velocity ($\langle \bar{U}_r \rangle$) at the impeller horizontal midplane ($z=0$), normalized by the impeller tip velocity, illustrating the angular deviations of $\langle U_r \rangle$ as calculated for the $T/D=3$ case at 1600 rpm at steady-state conditions.

[Color figure can be viewed in the online issue, which is available at wileyonlinelibrary.com.]

averaged radial velocity ($\langle U_r \rangle$) at the impeller horizontal midplane ($z=0$), as calculated for the $T/D=3$ case at 1600 rpm at steady-state conditions. To quantify the angular deviations and assess the validity of the axisymmetric assumption, we examined the standard deviation of the various flow-field variables along the angular coordinate. As an example, we present in Figure 6 contours of standard deviation values of the ensemble-averaged radial velocity along the angular coordinate ($SD_{\langle U_r \rangle}$), normalized with respect to the maximal averaged radial velocity at each radial cross section ($SD_{\langle U_r \rangle}/\bar{U}_{r,m}(r)$). As can be seen, the deviations caused by the blades and baffles are damped away from the sources leaving the majority of the jet domain with modest normalized standard deviation values (<10%). After examination of the various flow-field variables at steady-state conditions, we point out that the axisymmetric assumption can be applied with high confidence in the $1.4 < r/r_b < 2.4$ range for the $T/D=3$ case, respectively, in the $1.4 < r/r_b < 7$ range for the $T/D=9$ case.

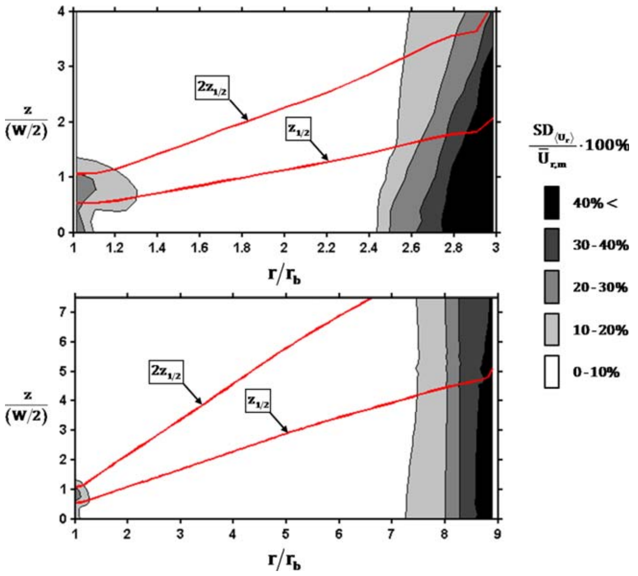

Figure 6. Contours of standard deviation values of the ensemble-averaged radial velocity along the radial coordinate ($SD_{\langle U_r \rangle}$), normalized with respect to the maximal averaged radial velocity at each radial cross section.

The upper diagram represents the $T/D=3$ numerical case whereas the lower diagram represents the $T/D=9$ numerical case, both at 1600 rpm.For reference, the corresponding numerical jet's half-width ($z_{1/2}$) and associated $2z_{1/2}$ value are marked as well. [Color figure can be viewed in the online issue, which is available at wileyonlinelibrary.com.]

The applicability of the axisymmetric assumption can be also extended to the $1 < r/r_b < 1.4$ range under the constraint of time-averaged statistics at fixed spatial locations (laboratory frame of reference). This is based on the reasonable assumption that at the vicinity of the impeller blades, where the effect of the baffles is modest and the deviations caused by the blades and associated trails are periodic,[53] the time-coordinate and angle-coordinate are directly related. This is also supported, to a large extend, by the good agreement between our model prediction and the experimental results in this region. Note that both time-averaging and angle-averaging are widely used in both numerical and experimental stirred tank studies,[14,27,45] methods which are suitable for analysis and characterization of mixing processes that involves physical mechanisms with characteristic time scales larger than the time scale of the blade passage ($(\text{blades} \cdot N)^{-1}$, ~6 ms when using the six-blade Rushton turbine at 1600 rpm).

In the following sections, we restrict our analysis to the $1 < r/r_b < 2.4$ range in the $T/D=3$ configuration, respectively, to the $1 < r/r_b < 5$ range in the $T/D=9$ case.

Prediction of the averaged radial velocity

As can be implied from the theoretical section, the prediction of $\bar{U}_r$ is of great importance as it is related to the determination of $\overline{u_r^2}$, k, ε, and ν_T. Moreover, it determines the residence time in this region. Following the theoretical section, viewing the impeller's discharge zone as a jet suggests two domains for describing the averaged radial velocity: before and after the potential core boundary (r_c). In the first, $\bar{U}_{r,m}$ and $z_{1/2}$ hardly change whereas in the second $\bar{U}_{r,m}$ decrease significantly while $z_{1/2}$ increase linearly (see Eqs. 8 and 9). This is evident from the plot of the normalized $\bar{U}_{r,m}$ and $z_{1/2}$ along the radial coordinate (see Figures 7–9).

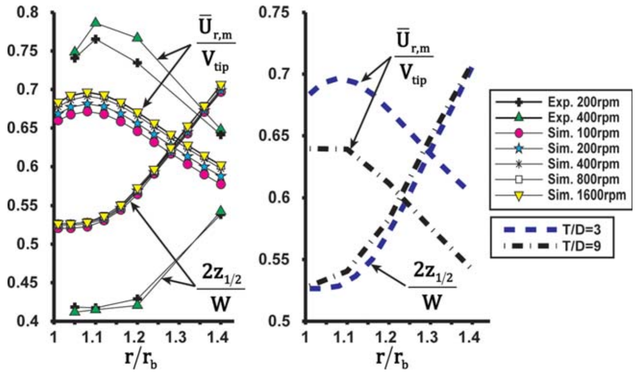

Figure 7. Computed and measured variation of $\bar{U}_{r,m}(r)$ and $z_{1/2}$ along the radial coordinate close to the impeller's tip.

Left diagram represents the $T/D=3$ case at various rotational speeds whereas diagram on right represents the 1600 rpm case at various T/D ratios (simulations only). [Color figure can be viewed in the online issue, which is available at wileyonlinelibrary.com.]

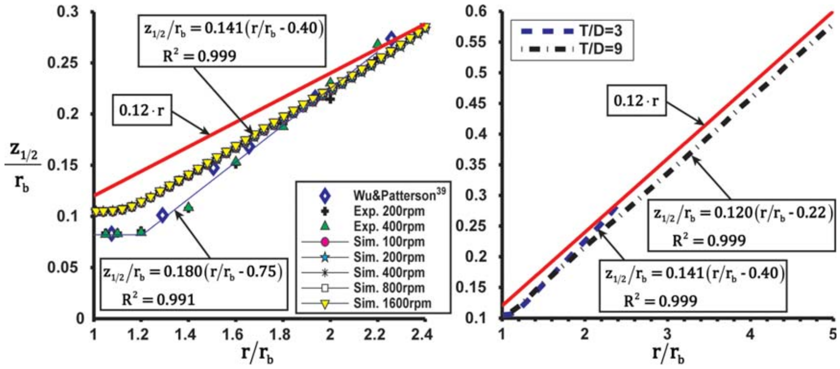

Figure 8. Computed and measured jet's half-width variation along the radial coordinate compared with asymptotic prediction ($z_{1/2}$=0.12r).

Left diagram represents the T/D=3 case at various rotational speeds whereas the right diagram represents the 1600 rpm case at various T/D ratios (simulations only). [Color figure can be viewed in the online issue, which is available at wileyonlinelibrary.com.]

The potential core, located close to the impeller tip, can be clearly identified in Figure 7. Its boundary (r_c) is evaluated to be located at r/r_b=1.2, independent of rotational speed and tank diameter. The last implies negligible wall effects. This value (r/r_b=1.2) corresponds to the minimal radial location beyond which the second derivative of $z_{1/2}$ remains relatively constant and equal to a zero value. Unlike common turbulent jets which have relatively uniform velocity profile at the potential core, the axial profile of the averaged radial velocity were found to be self-similar in this region (shown later on in Figure 10). Except for that and for the slight increase in $\bar{U}_{r,m}$, the potential core of the investigated system exhibits great resemblance to potential core of common turbulent jets. Its existence is also evident from previously published experimental and numerical results in which the measurement interval in the radial direction was small enough to capture this feature,[37,54,55] that is, the radial measurement grid consisted of more than one measurement point in the region $1 < r/r_b < 1.2$. After convincing that the potential core is distinct, let us now discuss quantitatively the jet's half-width and decay rate of the averaged radial velocity beyond r_c.

The jet's half-width ($z_{1/2}$) variation along the radial coordinate agrees well qualitatively with the linear theoretical prediction (see Figure 8 and Eq. 9). The spreading rate (i.e., S, the variation of $z_{1/2}$ along the radial coordinate) is indeed constant beyond r_c and independent of rotational speed. Nevertheless, the numerical results indicate it is dependent on the ratio T/D. Starting with S=0.141 for the T/D=3 numerical case and up to S=0.120 for the T/D=9 case. While the $k-\varepsilon$ model is known to exhibit higher spreading rates in jets compared to experimental results,[56] we received the opposite behavior for this system. The experimental results (T/D=3) provided S=0.180, significantly larger than the corresponding numerical value. The deviation between the two is attributed to the assumptions inherent in using the $k-\varepsilon$ turbulent model (e.g., isotropic flow). It is interesting to note that the spreading rate of the T/D=9 numerical case is very similar to the common value of simple turbulent jets. This is expected as wall effects become negligible for such large reactors. The values reported in the literature for the simple radial-jet system are very sparse,[36,57–61] leading to an average of 0.11 with approximately maximal deviation of 10%. The spreading rate values of the round and plane jet geometries, values which have been validated, are considered to be around 0.1–0.12.[47,62] This might imply that the spreading rate of radial impellers might be unique to the impeller used. The virtual origin (i.e., r_v, see Eq. 4) is located at r/r_b =0.40 and r/r_b=0.22 for the T/D=3 and T/D=9 numerical cases, respectively; whereas at r/r_b=0.75 for the experimental results. These values are high relative to the common stirred tank geometry (T/D=3) thus implying that very large tank diameters are required for the impeller's jet to become perfectly self-similar. Nevertheless, perfect self-similarity is not required for satisfactory prediction of the turbulent jet properties, as will be shown in this work.

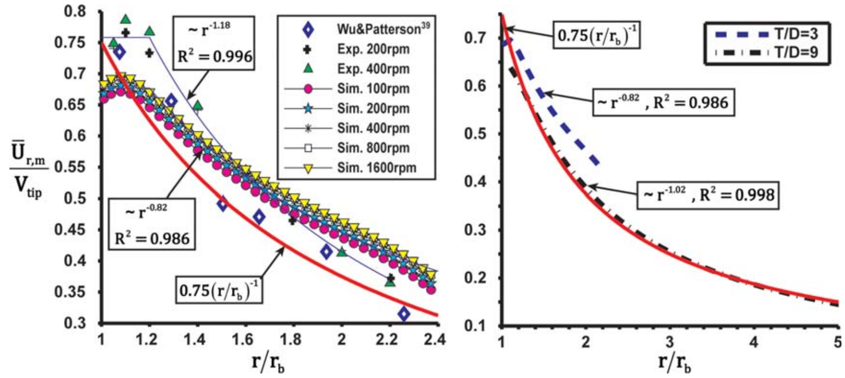

Figure 9. Computed and measured variation of the normalized averaged radial velocity at z=0 along the radial position ($\bar{U}_{r,m}(r)$).

Left diagram represents the T/D=3 case at various rotational speeds whereas the right diagram represents the 1600 rpm case at various T/D ratios (simulations only). [Color figure can be viewed in the online issue, which is available at wileyonlinelibrary.com.]

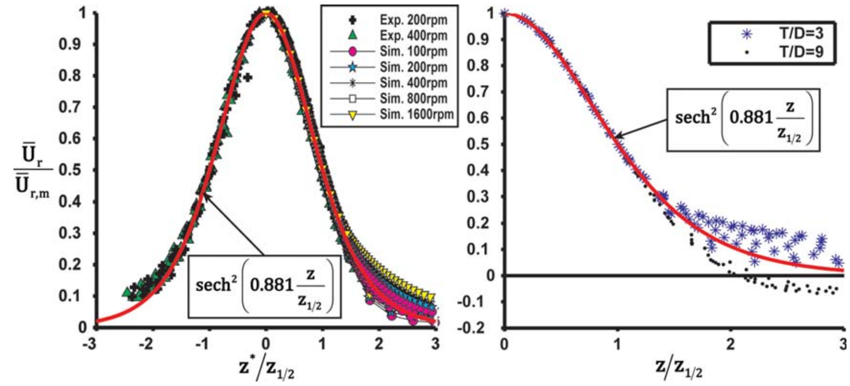

Figure 10. Computed and measured axial-distribution profiles of the averaged radial velocity across the jet ($r/r_b=1.05, 1.1, 1.2, 1.4, 1.6, 1.8, 2$, and 2.2).

Left diagram represents the $T/D=3$ case at various rotational speeds whereas the right diagram represents the 1600 rpm case at various T/D ratios (simulations only). [Color figure can be viewed in the online issue, which is available at wileyonlinelibrary.com.]

Both numerical and experimental results follow the qualitative physical behavior of the jet's half-width (described mathematically by Eq. 9). From the statistical point of view, both methods should have provided the same velocity flowfield. This suggests that the deviation may be attributed to the assumptions inherent in using the $k-\varepsilon$ turbulent model (e.g., isotropic flow).

The decay rate of $\bar{U}_{r,m}$ in ZEF along the radial coordinate is presented in Figure 9, and is fitted to a scaling of the form r^{-b} (starting from $r > r_c$). It exhibits negligible dependence on rotational speed (up to 5% difference) while according to the numerical investigation it varies with T/D. At the common geometry ($T/D=3$), it scales as $\sim 1/r^{0.82}$ and $\sim 1/r^{1.18}$ for the numerical and experimental cases, respectively; while for the $T/D=9$ case, it scales as $\sim 1/r^{1.02}$. Again, the value of the $T/D=9$ case approaches to the common value of the free radial-jet, $\bar{U}_{r,m} \sim 1/r$.

The axial-distribution profiles of the averaged radial velocity were found to exhibit very good self-similarity on the jet's core ($|z/z_{1/2}| \leq 1$), as can be seen in Figure 10. The numerical results achieved were symmetrical relative to the symmetry plane ($z=0$) whereas the experimental results showed small axial shifts (up to $0.25z/z_{1/2}$). Therefore, for clarity of presentation only the positive side of the numerical profiles is shown ($z/z_{1/2} \geq 0$) whereas the experimental ones are complete and presented using an adjusted axial coordinate (denoted by z^*), centered by the axial location of the maximal radial velocity of the radial velocity axial-distribution profile. As can be seen, up to $|z/z_{1/2}|=1$ the profiles collapse into one curve which correspond to the theoretical curve, whereas for $|z/z_{1/2}| > 1$ the profiles start to scatter and deviate from the theoretical curve. The deviation is attributed to the assumption of a constant turbulent viscosity whereas the scattering is considered reasonable compared with experimental results of common turbulent jets.[47,62] Note that with the increase in tank to impeller diameter ratio the scattering decrease significantly and becomes negligible. One should also notice that the ambient flow far from the jet (i.e., $|z/z_{1/2}| > 2.5$), for the $T/D=3$ case, exhibits a coflow behavior (i.e., the radial velocity is positive) relative to the impeller's jet whereas a weak counter flow (i.e., the radial velocity is negative) for the $T/D=9$ case. This behavior aligns with the numerical result in which the radial velocity decay rate is slower for the $T/D=3$ case.

It can be concluded that the behavior of $\bar{U}_r$ at the impeller's discharge zone is in accordance with the theory of turbulent jets; that is, there exist two domains—a potential core, in which $\bar{U}_r$ is almost constant, while beyond it the spreading rate is linear and the decay rate is of the form r^{-b}.

Prediction of $\overline{u_r^2}$, k, and ε in the ZFE

The prediction of k and ε is of great importance for industrial applications. Obtaining these parameters is usually more complicated and its accuracy is smaller than the ones related to the averaged velocity. Therefore, being able to predict these parameters based on the averaged radial velocity can reduce these drawbacks.

Following Theoretical Section, the prediction of these parameters is divided into two regions: in the ZFE ($r_b < r < r_z$) the axial-distribution profiles of these parameters develop to the final similarity profiles of the second zone. This is evident experimentally from the axial-distribution profiles of the normalized $\overline{u_r^2}$ at different radial positions (Figure 11). The ZFE is evaluated to span up to $r/r_b=1.6$ where the axial-distribution profiles of $\overline{u_r^2}$ (normalized by V_{tip}) exhibits three maxima points. The theoretical prediction presented at the ZFE (Eq. 16, using Eq. 10 and $\bar{U}_{r,m,b}/V_{\text{tip}}=0.75$ as was suggested earlier (see Eq. 12) was fitted by $A_u(r)$ (increases monotonically in the ZFE). Qualitatively, it can be seen that the model predicts well the evolvement of $\overline{u_r^2}$. The three maxima points approach each other to produce flat hat self-similar profile. To emphasis this point, the axial-distribution profiles of $\overline{u_r^2}$ (normalized by $\overline{u_{r,m}^2}$) beyond $r/r_b=1.6$ ($r/r_b=1.6$, 1.8, 2, and 2.2) were also shown along with the self-similar profile of $\bar{U}_r$ ($sech^2\left(0.881z/z_{1/2}\right)$). Quantitatively, at the vicinity of the impeller's blade, there is good agreement between the model prediction and the experimental results. The axial location of the three maxima points is well predicted along the region. With increasing radial position, the agreement between the two reduces. The theoretical profile becomes wider and exhibits moderate delay relative to the experimental one. The last is also evident from differences in the ZFE-ZEF boundary ($r_z=1.6$ and 2 corresponding to the experimental and theoretical values, respectively).

In Figure 12, we present comparison between the model prediction of k and ε (Eqs. 17 and 18, respectively) and experimental results at the ZFE region ($r/r_b=1.07$ and 1.2, corresponding to data from Wu and Patterson[39] and Escudie and Line,[27] respectively). The parameters fitting used for this purpose were $A_k=0.25(=A_u)$, $A_k=0.375(=A_u)$ (for the two

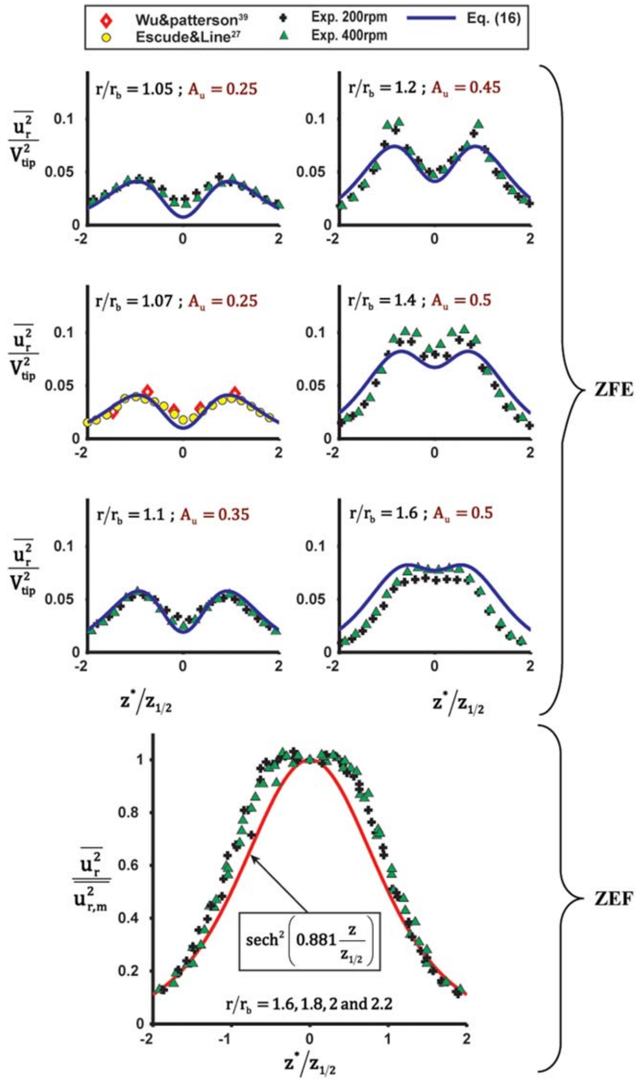

Figure 11. Measured axial-distribution profiles of the normalized $\overline{u_r^2}$ at different radial positions, showing the development with radial position in the ZFE and the asymptotic (self-similar) distribution in the ZEF.

[Color figure can be viewed in the online issue, which is available at wileyonlinelibrary.com.]

datasets) and $A_\varepsilon=0.085(\approx (0.5A_u)^{3/2})$. As the experimental half-width ($z_{1/2}$) at $r/r_b=1.2$ could not be extracted from the reported results, we used the experimental half-width ($z_{1/2}$) at $r/r_b=1.07$ of the same reference. This is with accordance to our perception in which $z_{1/2}$ is approximately constant up to $r/r_b=1.2$ (see Figure 8). It can be seen that there is good agreement between the model prediction and the experimental results including prediction of the three maxima points. Note that the data taken from Wu and Patterson[39] and Escudie and Line[27] was obtained using different tank sizes ($H=T=0.27$m and 0.45 m, respectively) and different impeller clearance ($C=H/3$) as well as with different rotational speeds (200 and 150 rpm, respectively) than ours ($H=T=0.3$m, $C=$H$/2$ using 200 and 400 rpm).

Prediction of v_T, k, and ε in the ZEF

In this section, we focus on the region beyond $r/r_b=1.6$ where the pseudoturbulence is known to be negligible.[39] Therefore, it is adequate to use our angle-averaged steady-state numerical results to validate the theory prediction of v_T, k, and ε in this region. Nevertheless, it should be noted that the numerical results presented in this section include both the random and the periodic turbulence.

The variation of the normalized turbulent kinetic energy ($k/V_{\rm tip}^2$) and the normalized turbulent kinetic energy dissipation rate ($\varepsilon/\left(V_{\rm tip}^3/D\right)$) at $z=0$ show that both k and ε scale according to Eq. 5 for $r/r_b > 1.6$ (Figures 13 and 14). The departure of the theoretical prediction from simulation results occurs in accordance with the evaluation of ZFE–ZEF boundary of the previous section. It can be also noticed that the values $k_{m,b}=0.158$ and $\varepsilon_{m,b}=0.061$ corresponds to the numerical values obtained by Kresta and Wood[25] for the free radial-jet. This yields further support to our view of the impeller's jet: (1) that the jet should be divided into two regions, (2) that characterizing the impeller's jet with respect to the radial coordinate is applicable. It should be stressed that by conducting extrapolation of both k and ε while starting from the impeller tip is physically incorrect, a practice that can result with significant error at the far field.

From the scaling of k and ε, it is evident that the turbulent viscosity is indeed constant in this region. The FLUENT code uses the $k-\varepsilon$ turbulence model to portray the k and ε fields, from which the turbulent viscosity is estimated via $v_T=0.09k^2/\varepsilon$. Using our derivation, the turbulent viscosity can be predicted from Eq. 7 in a semianalytical form. This prediction can be easily verified using the numerical values

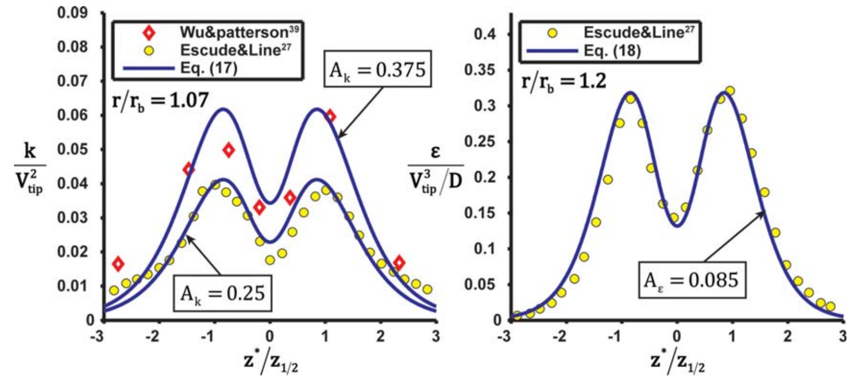

Figure 12. Measured and predicted axial-distribution profiles of the normalized *k* (left hand curve) and ε (right hand curve) at $r/r_b=1.07$ and 1.2 using data from Wu and Patterson[39] and Escudie and Line,[27] respectively.

[Color figure can be viewed in the online issue, which is available at wileyonlinelibrary.com.]

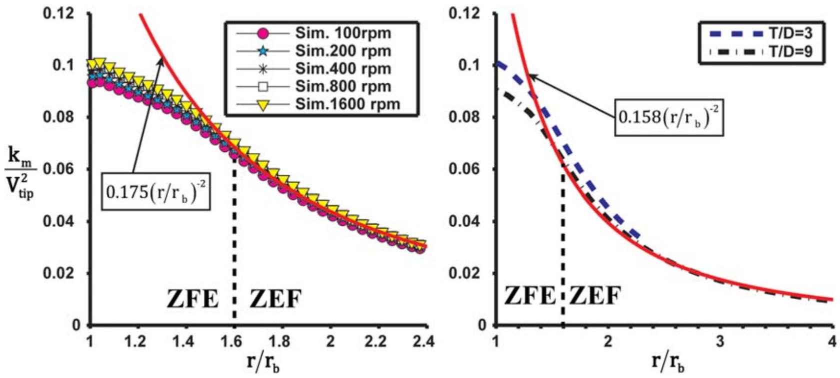

Figure 13. Variation of the normalized turbulent kinetic energy at $z=0$ along the radial coordinate.

Left hand curve represents the $T/D=3$ numerical case at various rotational speeds whereas the right hand curve represents the 1600 rpm numerical case at various T/D ratios. [Color figure can be viewed in the online issue, which is available at wileyonlinelibrary.com.]

of $\bar{U}_{r,m}$, $z_{1/2}$, and S (see Figures 8 and 9) to provide moderate relative error at the centerline of the impeller's jet (up to 20%). This prediction is of great importance as it enables to predict the turbulent viscosity in the impeller's jet domain using only few measurements of the averaged radial velocity at this region.

Summary

Following jet theory and the general theoretical framework of scalar dispersion in turbulent shear flows, we introduce a new perspective of the impeller's jet, now comprised of two main regions: the ZFE and the ZEF as presented in Figure 1. In Tables 1 and 2, we summarize our model where the real turbulent flow-field properties in these regions can be predicted using a few calibration measurements in the impellers' discharge zone. For example, only a few radial velocity profiles are required to determine the spreading rate (S) and the virtual origin (r_v). The pumping number (N_q) can be used with Eq. 12 to determine the maximal radial velocity at the impellers tip ($\bar{U}_{r,m,b}$) and the potential core boundary (r_c). As measurements of the radial velocity contain quantitative information of the normal Reynolds-stress in the radial direction ($\overline{u_r^2}$), the proportionality parameter A_u can be determined directly, whereas A_k and A_ε can be assessed accordingly. We can determine the ZFE-ZEF boundary (r_z) based on the radial location at which the parameter A_u starts to decrease. This is sufficient to predict the real turbulent flow-field ($\bar{U}_r$, k, ε, and ν_T) in the discharge zone of the impeller.

We use experimental LDA measurements and 3-D numerical calculations to validate our formulation of the impeller discharge zone in terms of ZFE and ZEF regions. In contrast, previous models in this field have not addressed the ZFE. Previous work viewed the impeller's jet as a fully developed jet starting from the impeller's tip, a practice that is physically incorrect. In such methods, the resulting problem is that extrapolation, of both k and ε from the impeller's tip, results in significant relative errors (see Figures 13 and 14).

The discoveries, methods, and analysis from our theoretical framework portend significant industrial importance and interest, for the following particular reasons:

1. As our theoretical model is scalable, it is well suited to a variety of industrial applications: the flow-field parameters can be tailored according to the required operational task, including changes in the system size and rotational speed of the impeller.
2. Industrial operators can predict the turbulent diffusivity of scalars (Γ_T) inside this region (e.g., temperature, concentration, etc.) using the turbulent viscosity and the Schmidt number ($Sc_T=\nu_T/\Gamma_T$, known to be bounded between 0.5 and 1.5).[63] Such results can be used for a multitude of design purposes, such as installation of temperature sensors for safety purposes.
3. Our proposed model can be used to approximate mixing rates, which assists industrial concerns in assessing reactive flow with reactants fed in the vicinity of the discharge jet.

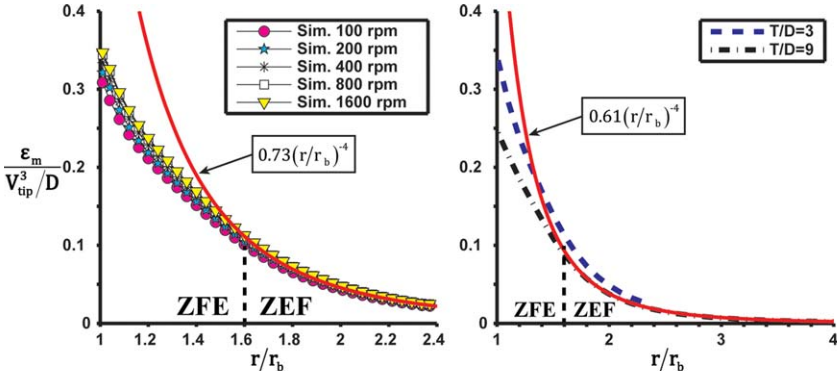

Figure 14. Variation of the normalized turbulent kinetic energy dissipation rate at $z=0$ along the radial coordinate.

Left hand curve represents the $T/D=3$ numerical case at various rotational speeds whereas the right hand curve represents the 1600 rpm numerical case at various T/D ratios. [Color figure can be viewed in the online issue, which is available at wileyonlinelibrary.com.]

In summary, we are motivated to continue to push semianalytical approaches to improve modeling of impellers in stirred tanks.

Acknowledgment

This research has been subsidized by the research project No. GA CR P101/12/2274 and RVO: 67985874.

Notation

A_u = coefficient of proportionality for $\overline{u_r^2}$, see Eq. 16
A_k = coefficient of proportionality for k, see Eq. 17
A_ε = coefficient of proportionality for ε, see Eq. 18
C = impeller off-bottom clearance, m
D = impeller diameter, m
Γ_T = the turbulent diffusivity of scalar
e = radius of a tangential jet source, also express the asymptotic ratio of the radial to angular momentum flux in the radial direction, m
H = tank height, m
k = turbulent kinetic energy, $m^2\ s^{-2}$
l_k = Kolmogorove length scale, m
N = impeller rotational speed
N_q = impeller's pumping number, Q_p/ND^3
Re = impeller's Reynolds number, ND^2/ν
R^2 = coefficient of determination
r_c = potential core boundary
r_b = impeller radius
r_v = virtual origin of the linear spreading
r_z = radial boundary between the ZFE and the ZEF
S = spreading rate defined by Eq. 2
SD_{U_r} = standard deviation of the ensemble-averaged radial velocity
Sc_T = the turbulent Schmidt number, $Sc_T = \nu_T/D_T$
Q_p = impeller's pumping capacity, $m^3\ s^{-1}$
T = tank diameter, m
$\overline{u_r^2}$ = the normal Reynolds-stress in the radial direction, $m^2\ s^{-2}$
$\bar{U}_r$ = angle-averaged mean radial velocity, $m\ s^{-1}$
U_r = ensemble-averaged radial velocity, $m\ s^{-1}$
V_{tip} = impeller's tip velocity, $\pi ND\ m\ s^{-1}$
W = impeller blade width, m
z^* = adjusted axial coordinate, with origin at the axial location (z) of the maximal radial velocity ($\bar{U}_{r,m}$) of the radial velocity axial-distribution profile ($\bar{U}_r(z)$)
$z_{1/2}$ = jet's half-width, defined by Eq. 1
ZFE = zone of flow establishment
ZEF = zone of established flow
ν = molecular viscosity, $m^2\ s^{-1}$
ν_T = turbulent viscosity, $m^2\ s^{-1}$
ε = turbulent kinetic energy dissipation rate, $m^2\ s^{-3}$

Subscript

m = implying for the impeller symmetry plane ($z=0$)
b = implying for the radial location where $r=r_b$

Abbreviations

LDA = Laser Doppler anemometry

Literature Cited

1. Hartmann H, Derksen J, Van den Akker H. Mixing times in a turbulent stirred tank by means of LES. *AIChE J.* 2006;52(11):3696–3706.
2. Jahoda M, Moštěk M, Kukuková A, Machoň V. CFD modelling of liquid homogenization in stirred tanks with one and two impellers using large eddy simulation. *Chem Eng Res Des.* 2007;85(5):616–625.
3. Montante G, Magelli F. Liquid homogenization characteristics in vessels stirred with multiple rushton turbines mounted at different spacings: CFD study and comparison with experimental data. *Chem Eng Res Des.* 2004;82(9):1179–1187.
4. Sha Z, Palosaari S, Oinas P, Ogawa K. CFD simulation of solid suspension in a stirred tank. *J Chem Eng Jpn.* 2001;34(5):621–626.
5. Dohi N, Takahashi T, Minekawa K, Kawase Y. Power consumption and solid suspension performance of large-scale impellers in gas–liquid–solid three-phase stirred tank reactors. *Chem Eng J.* 2004;97(2):103–114.
6. Murthy B, Ghadge R, Joshi J. CFD simulations of gas-liquid-solid stirred reactor: prediction of critical impeller speed for solid suspension. *Chem Eng Sci.* 2007;62(24):7184–7195.
7. Torbacke M, Rasmuson ÅC. Influence of different scales of mixing in reaction crystallization. *Chem Eng Sci.* 2001;56(7):2459–2473.
8. Pastor L, Mangin D, Barat R, Seco A. A pilot-scale study of struvite precipitation in a stirred tank reactor: conditions influencing the process. *Bioresour Technol.* 2008;99(14):6285–6291.
9. Guay M, Dochain D, Perrier M. Adaptive extremum seeking control of continuous stirred tank bioreactors with unknown growth kinetics. *Automatica.* 2004;40(5):881–888.
10. Arriaga S, Muñoz R, Hernández S, Guieysse B, Revah S. Gaseous hexane biodegradation by fusarium solani in two liquid phase packed-bed and stirred-tank bioreactors. *Environ Sci Technol.* 2006;40(7):2390–2395.
11. Paul EL, Atiemo-Obeng VA, Kresta SM. Handbook of Industrial Mixing: Science and Practice. Hoboken, NJ: Wiley, 2004.
12. Ciofalo M, Brucato A, Grisafi F, Torraca N. Turbulent flow in closed and free-surface unbaffled tanks stirred by radial impellers. *Chem Eng Sci.* 1996;51(14):3557–3573.
13. Hartmann H, Derksen J, Van den Akker H. Macroinstability uncovered in a rushton turbine stirred tank by means of LES. *AIChE J.* 2004;50:2383–2393.
14. Soos M, Kaufmann R, Winteler R, Kroupa M, Lüthi B. Determination of maximum turbulent energy dissipation rate generated by a rushton impeller through large eddy simulation. *AIChE J.* 2013; 59(10):3642–3658.
15. Ng K, Fentiman N, Lee K, Yianneskis M. Assessment of sliding mesh CFD predictions and LDA measurements of the flow in a tank stirred by a rushton impeller. *Chem Eng Res Des.* 1998;76(6):737–747.
16. Ranade V, Perrard M, Le Sauze N, Xuereb C, Bertrand J. Trailing vortices of rushton turbine: PIV measurements and CFD simulations with snapshot approach. *Chem Eng Res Des.* 2001;79(1):3–12.
17. Joshi JB, Nere NK, Rane CV, Murthy BN, Mathpati CS, Patwadhan AW, Ranade VV. CFD simulation of stirred tanks: comparison of turbulence models. *Part I: radial flow impellers. Can J Chem Eng.* 2011;89(1):23–82.
18. Riley N. Radial jets with swirl. *Q J Mech Appl Math.* 1962;15(4): 435–458.
19. O'Nan M, Schwarz W. The swirling radial free jet. *Appl Sci Res.* 1966;15(1):289–312.
20. Drbohlav J, Fořt I, Máca K, Ptáček J. Turbulent characteristics of discharge flow from the turbine impeller. *Collect Czech Chem Commun.* 1978;43(12):3148–3162.
21. Kratěna J, Fořt I, Brůha O. Dynamic effect of discharge flow of a rushton turbine impeller on a radial baffle. *Acta Polytech.* 2001;41:58–63.
22. Talaga J, Fořt I. The velocity field in the discharge stream from a rushton turbine impeller. In proceedings of: *The 14th European Conference on Mixing*, September, 2012, Warszaw, Poland. 467–472.
23. Kolář V, Filip P, Curev A. The swirling radial jet. *Appl Sci Res.* 1982;39(4):329–335.
24. Kolář V, Filip P, Curev A. Hydrodynamics of a radially discharging impeller stream in agitated vessels. *Chem Eng Commun.* 1984;27(5–6):313–326.
25. Kresta SM, Wood PE. Prediction of the three-dimensional turbulent flow in stirred tanks. *AIChE J.* 1991;37(3):448–460.
26. Van't Riet K, Bruijn W, Smith JM. Real and pseudo-turbulence in the discharge stream from a rushton turbine. *Chem Eng Sci.* 1976; 31(6):407–412.
27. Escudie R, Line A. Experimental analysis of hydrodynamics in a radially agitated tank. *AIChE J.* 2003;49(3):585–603.
28. Ben-Nun R, Sheintuch M. Characterizing turbulent jet properties of radial discharge impeller: potential core, spreading rate and averaged flow field parameters. *The 9th European Congress of Chemical Engineering*. Hague, Netherlands, 2013.
29. Tamburini A, Cipollina A, Micale G, Brucato A. Measurements of njs and power requirements in unbaffled bioslurry reactors. *Chem Eng Trans.* 2012;27:343–348.
30. Chen CJ, Nikitopoulos CP. On the near field characteristics of axisymmetric turbulent buoyant jets in a uniform environment. *Int J Heat Mass Transfer.* 1979;22(2):245–255.
31. Kuang J, Hsu C, Qiu H. Experiments on vertical turbulent plane jets in water of finite depth. *J Eng Mech.* 2001;127(1):18–26.
32. Wen-xin LWH. Prediction of the characteristics for ZEF of buoyant jets [J]. *J Hydrodynam.* 1990;2:003.

33. Tennekes H, Lumley JL. A First Course in Turbulence. Cambridge: The MIT press, 1972.
34. Rajaratnam N. Developments in Water Science, Vol. 5. Amsterdam: Elsevier scientific publishing company, 1976.
35. Rodi W. The Prediction of Free Turbulent Boundary Layers by Use of a Two-Equation Model of Turbulence. London, UK: University of London, 1972.
36. Tanaka T, Tanaka E. Experimental study of a radial turbulent jet: 1st report, effect of nozzle shape on a free jet. *Bull JSME.* 1976; 19(133):792–799.
37. Lee K, Yianneskis M. Turbulence properties of the impeller stream of a rushton turbine. *AIChE J.* 1998;44(1):13–24.
38. Chatwin PC, Sullivan PJ. A simple and unifying physical interpretation of scalar fluctuation measurements from many turbulent shear flows. *J Fluid Mech.* 1990;212:533–556.
39. Wu H, Patterson GK. Laser-doppler measurements of turbulent-flow parameters in a stirred mixer. *Chem Eng Sci.* 1989;44(10):2207–2221.
40. Holland FA, Chapman FS. *Liquid Mixing and Processing in Stirred Tanks.* NY: Reinhold Publishing Corporation, 1966.
41. Gillissen JJJ, Van den Akker HEA. Direct numerical simulation of the turbulent flow in a baffled tank driven by a rushton turbine. *AIChE J.* 2012;58(12):3878–3890.
42. ANSYS Inc., *ANSYS Fluent User's Guide.* Canonsburg, PA; 2010.
43. Launder B, Sharma B. Application of the energy-dissipation model of turbulence to the calculation of flow near a spinning disc. *Lett Heat Mass Transfer.* 1974;1:131–137.
44. Launder BE, Spalding DB. The numerical computation of turbulent flows. *Comput Methods Appl Mech Eng.* 1974;3(2):269–289.
45. Coroneo M, Montante G, Paglianti A, Magelli F. CFD prediction of fluid flow and mixing in stirred tanks: numerical issues about the RANS simulations. *Comput Chem Eng.* 2011;35(10):1959–1968.
46. Deglon DA, Meyer CJ. CFD modelling of stirred tanks: numerical considerations. *Miner Eng.* 2006;19(10):1059–1068.
47. Pope SB. Turbulent Flows. Cambridge, UK: Cambridge University Press, 2000.
48. Reynolds WC, Hussain AKMF. The mechanics of an organized wave in turbulent shear flow. Part 3. Theoretical models and comparisons with experiments. *J Fluid Mech.* 1972;54(02):263–288.
49. Montante G, Lee K, Brucato A, Yianneskis M. Experiments and predictions of the transition of the flow pattern with impeller clearance in stirred tanks. *Comput Chem Eng.* 2001;25(4):729–735.
50. Li Z, Bao Y, Gao Z. PIV experiments and large eddy simulations of single-loop flow fields in rushton turbine stirred tanks. *Chem Eng Sci.* 2011;66(6):1219–1231.
51. Motamedvaziri S, Armenante PM. Flow regimes and surface air entrainment in partially filled stirred vessels for different fill ratios. *Chem Eng Sci.* 2012;81:231–250.
52. Ben-Nun R, Marmur A, Sheintuch M. Symmetry breaking and hysteresis of the averaged flow field in stirred tank reactors with radial impellers. *The North American Mixing Forum (NAMF) XXIV Conference*, The Sagamore, Lake George, NY, 2014.
53. Rutherford K, Lee K, Mahmoudi S, Yianneskis M. Hydrodynamic characteristics of dual rushton impeller stirred vessels. *AIChE J.* 1996;42(2):332–346.
54. Yoon HS, Sharp KV, Hill DF, Adrian RJ, Balachandar S, Ha MY, Kar K. Integrated experimental and computational approach to simulation of flow in a stirred tank. *Chem Eng Sci.* 2001;56(23):6635–6649.
55. Wadnerkar D, Utikar RP, Tade MO, Pareek VK. CFD simulation of solid–liquid stirred tanks. *Adv Powder Technol.* 2012;23(4):445–453.
56. Chorny A, Zhdanov V. Turbulent mixing and fast chemical reaction in the confined jet flow at large schmidt number. *Chem Eng Sci.* 2012;68(1):541–554.
57. Wood P, Chen C. Turbulence model predictions of the radial jet—a comparison of κ-ϵ models. *Can J Chem Eng.* 1985;63(2):177–182.
58. Heskestad G. Hot-wire measurements in a radial turbulent jet. *J Appl Mech.* 1966;33:417–424.
59. Dwyer H. The turbulent radial jet. *J Fluid Mech.* 1976;75(part 3): 401–417.
60. Patel RP. Some measurements in radial free jets. *AIAA J.* 1979; 17(6):657–659.
61. Sun Z, Li W, Liu H. Study on the radial jet velocity distribution of two closely spaced opposed jets. *Int J Heat Fluid Flow.* 2009;30(6):1106–1113.
62. Lee JHW, Chu VH. Turbulent Jets and Plumes: A Lagrangian Approach. The Netherlands: Springer, 2003.
63. Baldyga J, Bourne JR. Turbulent Mixing and Chemical Reactions. New York: Wiley, 1999.

Appendix A: The Swirling-Radial-Jet

In this section, we briefly review and solve the turbulent swirling-radial-jet equations to derive expressions for the self-similar profile of $\bar{U}_r$ and the ν_T in the ZEF.

The implementation of assumptions (1)–(7) given in the theoretical section, results in the basic swirling-radial-jets equations[23]

$$\frac{\partial(r\bar{U}_r)}{\partial r}+\frac{\partial(r\bar{U}_z)}{\partial z}=0 \tag{A1}$$

$$\bar{U}_r\frac{\partial(\bar{U}_r)}{\partial r}+\bar{U}_z\frac{\partial(\bar{U}_r)}{\partial z}-\frac{\bar{U}_\theta^2}{r}=\nu_T\frac{\partial^2\bar{U}_r}{\partial z^2} \tag{A2}$$

$$\bar{U}_r\frac{\partial(\bar{U}_\theta)}{\partial r}+\bar{U}_z\frac{\partial(\bar{U}_\theta)}{\partial z}+\frac{\bar{U}_\theta\bar{U}_r}{r}=\nu_T\frac{\partial^2\bar{U}_\theta}{\partial z^2} \tag{A3}$$

These equations can be further reduced to the basic turbulent radial-jet equations with no swirl in a direction tangent to a cylinder of constant radius. The reduction is based on Riely's coordinate transformation[18] which is given by

$$\xi=\sqrt{r^2-e^2} \tag{A4}$$

where "e" is the virtual origin of the transformation (see Figure A1) expressing the cylinder constant radius (elaboration on the physical meaning of "e" can be found in Kresta and Wood[25]).

From geometrical considerations, the following relations can be derived

$$\bar{U}_r=\bar{U}_\xi\frac{\xi}{r};\quad \bar{U}_\theta=\bar{U}_\xi\frac{e}{r} \tag{A5}$$

which after substitution into Eqs. A1–A3 form the basic turbulent radial-jet equations (with no swirl) in the ξ direction

$$\frac{\partial(\xi\bar{U}_\xi)}{\partial \xi}+\frac{\partial(\xi\bar{U}_z)}{\partial z}=0 \tag{A6}$$

$$\bar{U}_\xi\frac{\partial(\bar{U}_\xi)}{\partial \xi}+\bar{U}_z\frac{\partial(\bar{U}_\xi)}{\partial z}=\nu_T\frac{\partial^2\bar{U}_\xi}{\partial z^2} \tag{A7}$$

with the boundary conditions given by

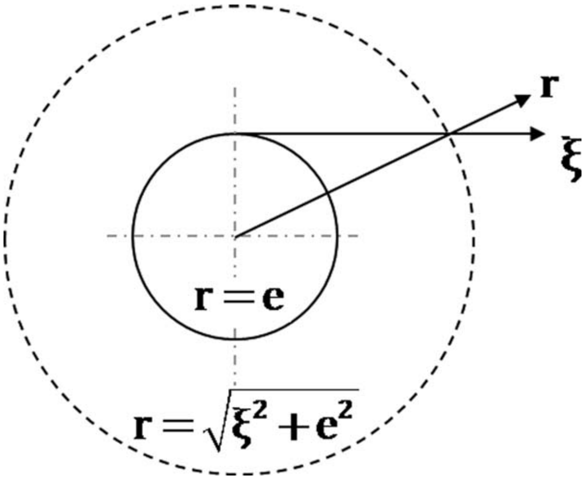

Figure A1. Schematic presentation of Riely's coordinate transformation for reduction of the turbulent swirling-radial-jet equations to the basic radial-jet equations with no swirl in a direction tangent to a cylinder of constant radius (ξ).

$$\lim_{z\to\pm\infty} \bar{U}_\xi = 0 \qquad \frac{\partial(\bar{U}_\xi)}{\partial z}\Big|_{z=0} = 0 \tag{A8}$$

$$\lim_{z\to\pm\infty} \frac{\partial(\bar{U}_z)}{\partial z} = 0 \qquad \bar{U}_z\big|_{z=0} = 0 \tag{A9}$$

To solve these equations, we follow the same procedure presented in the book "Turbulent Flows" for the round jet.[47] We start with introducing the stokes stream function $\psi(\xi, r)$ as

$$\bar{U}_\xi = \frac{1}{r}\frac{\partial\psi}{\partial z}; \qquad \bar{U}_z = -\frac{1}{r}\frac{\partial\psi}{\partial\xi} \tag{A10}$$

so that the continuity equation is automatically satisfied. Under the assumption of self-similar flow, the stream function can be represented by

$$\psi = v_T r G(\eta); \quad \eta = \frac{z}{\xi} \tag{A11}$$

where $G(\eta)$ is the self-similar function of ψ. From Eqs. A10 and A11, it follows that

$$\bar{U}_\xi = \frac{v_T}{\xi} G'; \qquad \bar{U}_z = \frac{v_T}{\xi}(\eta G' - G) \tag{A12}$$

where $G' = dG/d\xi$. Substituting Eq. A12 into Eqs. A6 and A7 and rearranging one obtains

$$GG'' + (G')^2 = -G''' \tag{A13}$$

Integrating Eq. A13 and using Eqs. A8 and A9 to determine the integration coefficients results with

$$\bar{U}_\xi = v_T 2b^2 \xi^{-1} \operatorname{sec}h^2(b\eta) = \bar{U}_{\xi,m} \operatorname{sec}h^2(b\eta) \tag{A14}$$

where b is a parameter, derived from the integration. This parameter can be determined from the definition of $z_{1/2}$ to provide

$$b = 0.881/S \tag{A15}$$

From Eq. A5 and Eqs. A14 and A15 it follows that

$$\frac{\bar{U}_r}{\bar{U}_{r,m}} = \operatorname{sec}h^2\left(0.881\frac{z}{z_{1/2}}\right) \tag{A16}$$

and

$$v_T = \frac{S \cdot \bar{U}_{r,m} \cdot z_{1/2}}{2(0.881)^2} \tag{A17}$$

where $\bar{U}_{r,m}$ scales as r^{-1}.

Manuscript received May 23, 2014, and revision received Nov. 26, 2014.